

Multi-scale time-resolved electron diffraction: A case study in moiré materials

C.J.R. Duncan,¹ M. Kaemingk,¹ W.H. Li,¹ M.B. Andorf,¹ A.C.
Bartnik,¹ A. Galdi,¹ M. Gordon,¹ C.A. Pennington,¹ I.V. Bazarov,¹ H.J.
Zeng,² F. Liu,² D. Luo,³ A. Sood,^{4,5} A.M. Lindenberg,⁶ M.W. Tate,⁷
D.A. Muller,^{8,9} J. Thom-Levy,¹⁰ S.M. Gruner,^{7,8} and J.M. Maxson¹

¹*Cornell Laboratory for Accelerator-Based Sciences and Education,
Cornell University, Ithaca, NY 14850, USA*

²*Department of Chemistry, Stanford University, Stanford, CA 94305, USA*

³*SLAC National Accelerator Laboratory, Menlo Park, CA 94205, USA*

⁴*Department of Mechanical and Aerospace Engineering,
Princeton University, Princeton, NJ 08540, USA*

⁵*Princeton Materials Institute, Princeton University, Princeton, NJ, 08540, USA*

⁶*Department of Materials Science and Engineering,
Stanford University, Stanford, CA, 94305, USA*

⁷*Laboratory of Atomic and Solid State Physics,
Cornell University, Ithaca, NY, 14853, USA*

⁸*Kavli Institute at Cornell for Nanoscale Science, Ithaca, NY 14853, USA*

⁹*School of Applied and Engineering Physics,
Cornell University, Ithaca, NY 14853 USA*

¹⁰*Laboratory for Elementary-Particle Physics,
Cornell University, Ithaca, NY 14853, USA*

arXiv:2206.08404v2 [physics.ins-det] 27 Jul 2023

Abstract

Ultrafast-optical-pump — structural-probe measurements, including ultrafast electron and x-ray scattering, provide direct experimental access to the fundamental timescales of atomic motion, and are thus foundational techniques for studying matter out of equilibrium. High-performance detectors are needed in scattering experiments to obtain maximum scientific value from every probe particle. We deploy a hybrid pixel array direct electron detector to perform ultrafast electron diffraction experiments on a WSe₂/MoSe₂ 2D heterobilayer, resolving the weak features of diffuse scattering and moiré superlattice structure without saturating the zero order peak. Enabled by the detector’s high frame rate, we show that a chopping technique provides diffraction difference images with signal-to-noise at the shot noise limit. Finally, we demonstrate that a fast detector frame rate coupled with a high repetition rate probe can provide continuous time resolution from femtoseconds to seconds, enabling us to perform a scanning ultrafast electron diffraction experiment that maps thermal transport in WSe₂/MoSe₂ and resolves distinct diffusion mechanisms in space and time.

I. INTRODUCTION

Ultrafast x-ray and electron scattering experiments are essential tools in the materials-by-design thrust of modern condensed matter physics and engineering, as they can probe far-from-equilibrium dynamic phenomena at atomic space and time scales [1–6]. In this discipline, technological improvements in probe quality (space/momentum and time/energy resolution) and probe detection (sensitivity, speed) are key to enabling the discovery of new non-equilibrium material functionality [7, 8].

Atomically thin moiré materials, such as twisted homobilayers or heterobilayers [9–15], present exciting opportunities for ultrafast study given the wide array of *equilibrium* quantum phenomena observed in these systems, including superconductivity and orbital magnetism, that are *tunable* with twist angle [16, 17]. Appropriately tuned ultrafast excitation may be a route to optical switching of these properties, as has been observed in other quantum materials [6, 18].

Many of the properties that make 2D materials physically interesting also pose significant challenges for ultrafast structural probes. Atomically thin films are inherently weak scat-

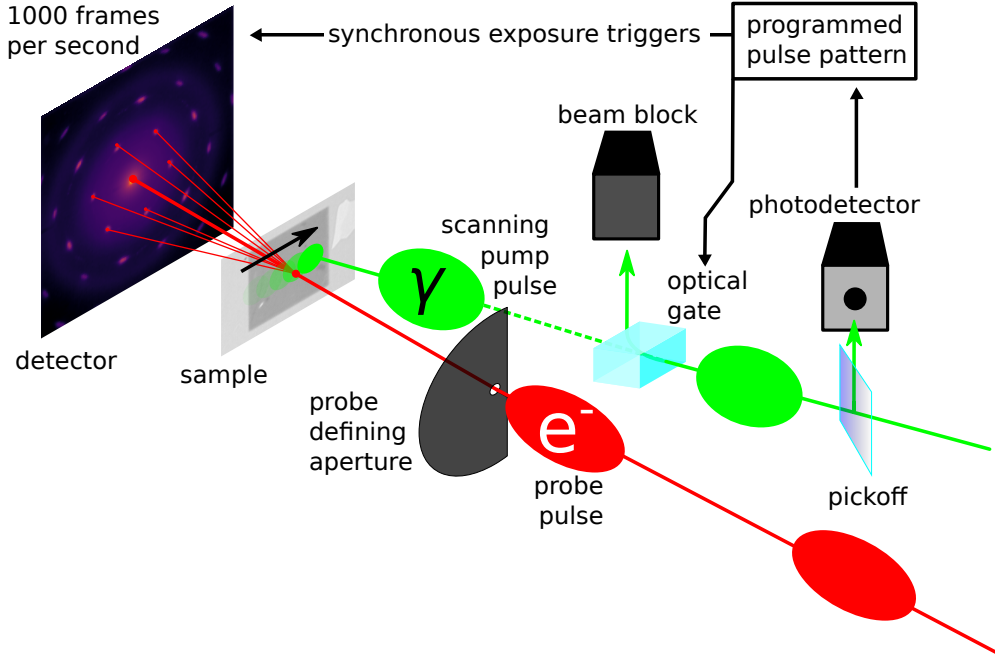


FIG. 1. Schematic of our ultrafast electron diffraction setup, which enables our femtosecond, micron-sized probe to measure both the spatial and temporal dependence of the sample response to pumping with femtosecond, 515 nm laser pulses. Pump pulses are independently gated, synchronously with detector triggering, allowing us to isolate individual probe pulses arriving from 10^{-13} to 10^{-3} s after the pump pulse.

terers and this challenge is compounded by the fact that compact ultrafast probes generally offer lower time-average flux than their non-time-resolved counterparts [19–21]. Further, important features in the information-rich diffraction patterns from these materials can be separated by many orders of magnitude in intensity: descending from the (0,0,0) peak, to Bragg scattering, to weaker satellite peaks caused by longer wavelength periodic lattice distortions (PLD), to yet weaker thermal diffuse scattering (TDS) [22]. In pump-probe ultrafast electron diffraction (UED), we seek to measure small changes in this already weak scattering. For example, important details of electron-phonon coupling can be found in parts per thousand modulation of scattering signals that in static diffraction are already at the 10^{-4} level of total beam current. Moiré materials exemplify this challenge, and could plausibly present correlated signatures of interlayer interactions in Bragg, PLD and TDS scattering, with tunable superstructure periodicity that can extend to tens of nm [10].

To meet the material-science need to investigate ultrafast evolution of diffraction features

across multiple intensity and length scales simultaneously – in the same scattering data set and with Poisson-limited experimental precision – requires bright probe sources and detectors with single-particle sensitivity and high dynamic range. Workhorse indirect detectors function by detecting light generated in a scintillator, which places limits on dynamic range, spatial resolution, and sensitivity [23–26]. The standard metric for detector performance is detective quantum efficiency (DQE): state-of-the-art indirect detectors offer DQE at best in the few tens of percent, whereas a purely shot noise limited detection system would have a DQE of unity [27]. Among devices that aim to overcome these limitations [28], direct detectors are now an established tool at x-ray user facilities [29–31], and enable computational imaging with state-of-the-art resolution in non-time-resolved electron microscopy [32, 33], higher energy resolution in electron-energy-loss spectroscopy [34], and higher spatial-resolution in electron cryo-microscopy [35].

The most common approach to direct electron detection is *pulse counting* [36], which saturates at one particle per pixel per relaxation period (order 100 ns) and thus cannot handle the large peak currents typical of UED experiments [19]. Integrating direct detectors, by comparison, accurately report the total probe-particle energy incident on each pixel and are uniquely suited for applications with high-intensity pulsed beams of sub-ps duration, such as UED [37].

The direct electron detector we employ in this work, the Electron Microscope Pixel Array Detector (EMPAD) has a DQE (at zero spatial frequency) of 0.95, with a signal to noise ratio for individual electron detection approaching 100 for 140 keV electrons. Its novel in-pixel, hybrid analog/digital circuitry simultaneously provides very high dynamic range, as described below [38].

Fluctuations in the probe current incident on the sample also limit precision when measuring scattering rates, even if the detector counts scattered particles perfectly. Causes include variation in laser power on the photocathode, changes in the quantum efficiency of the photocathode, and – critical in micro-diffraction – unavoidable jitter and drift in the probe beam position on the probe defining aperture. Fluctuations in probe current fail to oscillate around a time-independent mean: thus, experimental precision does not improve from simply averaging longer acquisitions.

Instead, the incident probe current often exhibits universal $1/f$ frequency dependence. The impact is severe when probing both real-space and reciprocal space features of the sample, as done in micro-diffraction experiments [39, 40]. In optical pump-probe modalities, such as absorption spectroscopy, high-frequency pulse chopping and lock-in detection is an essential technique that reduces frequency-dependent noise [41], but impossible to adopt in UED without a fast frame rate detector capable of measuring the reference signal at frequencies well above those of the noise sources.

Ultimately, sample lifetime under the stress of repeated pump-probe cycles imposes a physical bound on total experiment time. Therefore, reducing acquisition time by eliminating sources of noise (other than fundamental Poisson uncertainty) significantly increases the breadth of feasible pump-probe experiments.

Here we deploy the EMPAD integrating electron detector, with our high brightness keV ultrafast electron micro-diffraction beamline [39], to probe the out-of-equilibrium dynamics of a $\text{WSe}_2/\text{MoSe}_2$ moiré bilayer at long spatial periodicity (high resolution in reciprocal space) and ultrafast time scales [38, 39, 42, 43]. For the first time in UED, we resolve a 10 nm periodic moiré superlattice [44]. We integrate the superlattice signal without saturating the more intense Bragg peaks caused by angstrom scale interatomic spacing. We demonstrate that the 1 kHz detector frame rate enables a fast pulse chopping technique that drastically improves signal-to-noise in measurements of the sample response to ultrafast pumping.

The fast 1 kHz detector frame rate also enables a novel pulse-picking technique, which extends the range of timescales accessible in ultrafast pump-probe experiments beyond μs with fs precision. Implementations of pump-probe delays at the μs scale typically rely on electrical triggering, e.g., nanosecond Q-switched lasers or gain-switched diodes with picosecond pulse duration [45]. Femtosecond pulses, by increasing the peak laser field strength for the same deposited energy, have the potential to unlock interesting metastable behavior [46], and our method could resolve, e.g., THz frequency modulations μs after excitation. We demonstrate our pulse-picking technique with a micro-diffraction probe and map the diffusion of heat in our sample in space and time from initial fs ultrafast excitation, out to ms thermal relaxation, with μm spatial resolution. Experimental access to 100 μs timescales allows us to extract from our space-and-time-resolved data the thermal diffusivity of our

moiré sample.

II. RESULTS

A. Resolving moiré superstructure

Our beamline setup is summarized in Fig. 1 and Appendix A; additional details can be found in a previous work [39]. To take best advantage of the detector frame rate, we independently gate pump and probe pulse trains obtained from a femtosecond fiber-laser source with a repetition rate of 125 kHz. The pump wavelength in the experiments reported here is 515 nm. In micro-diffraction mode, depending on the beam coherence required to resolve the reciprocal space structure of interest, typical charges per pulse on target range from 10 to 1000 electrons.

A magnetic quadrupole lens triplet controls the angular magnification of the diffraction pattern on the detector. Lens settings are summarized by *camera length*: the hypothetical drift distance to the detector plane that would result in equivalent diffraction data.

Figure 2(a) shows a static diffraction pattern obtained from the WSe₂/MoSe₂ sample at short camera length. The six-fold symmetry of the diffraction pattern arises from the underlying symmetry of the WSe₂/MoSe₂ lattices. The logarithmic scale color bar includes over four orders of magnitude of contrast from the (0,0,0) peak to thermal diffuse scattering.

The EMPAD consists of a grid of 128×128 pixels each $150 \mu\text{m} \times 150 \mu\text{m}$ in size. Each pixel has a $500 \mu\text{m}$ thick reverse-biased silicon diode bump bonded to its own read-out electronic circuit. The well of each pixel can record up to 10^6 electron incidents per exposure, but the detector saturates at lower counts if the rate of incidents exceeds a threshold. Previous measurements performed with continuous beam illumination (*cw*) estimated this threshold rate to be 22 electrons per pixel per microsecond at our 140 keV beam energy. Surprisingly, in our pulsed experiments we observe saturation at the significantly higher rate of 60 electrons per pixel per sub-picosecond pulse, a result likely analogous to effects studied in the context of x-ray free electron laser applications, and discussed further in Appendix B. The EMPAD design is under active development and the latest iteration (not deployed in our experiments) increases the *cw* saturation level to 10^3 electrons per pixel per microsecond [47].

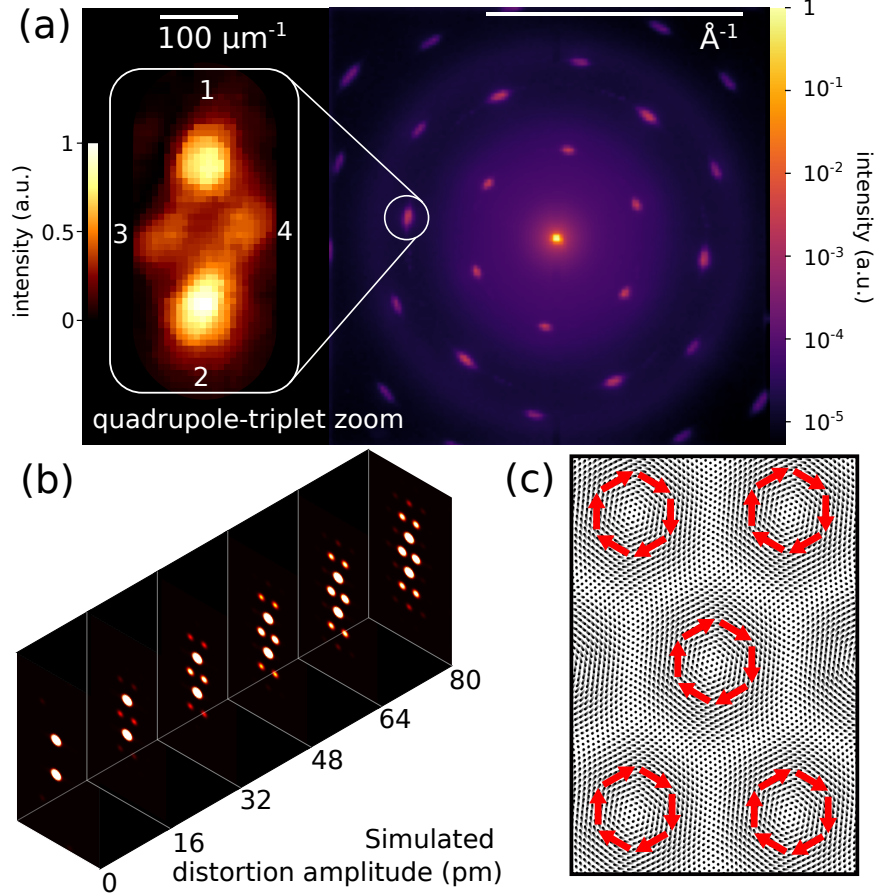


FIG. 2. (a) Logarithmic scale diffraction pattern obtained from $\text{WSe}_2/\text{MoSe}_2$ at short-camera length, demonstrating the EMPAD dynamic range. Inset left, a long camera-length diffraction difference pattern showing a single pair of moiré Bragg peaks, labeled 1 and 2: also visible, a pair of satellite peaks, labeled 3 and 4, with 10 nm periodicity. This inset image shows the absolute value of the difference in counts between a laser-pumped and unpumped sample at a delay of 4 ps: pumping enhances the contrast between the satellite peaks and the tails of the main Bragg peaks. The effect of beam chopping on the experimental uncertainty of peaks labeled 1 and 2 is shown in Fig. 5. Detector camera length is varied with a magnetic quadrupole lens triplet. At the camera length shown inset, the width of one detector pixel is 2.6×10^{-3} reciprocal lattice units (rlu) and the electron beam spot size on the detector is 1.1×10^{-2} rlu, where $1 \text{ rlu} := 0.30 \text{ \AA}^{-1}$. (b) Simulated diffraction patterns as a function of period-lattice-distortion (PLD) amplitude; PLD is driven by interlayer interaction between WSe_2 and MoSe_2 . (c) Simulated moiré lattice visualized in real space; red arrows indicate direction of local atomic displacement.

The inset to Fig. 2(a) shows a long-camera-length diffraction difference pattern isolating a single pair of Bragg peaks ($\bar{1}\bar{1}20$), aligned vertically in the image, with two additional satellite peaks visible, aligned horizontally. The difference pattern is formed by subtracting pumped exposures from unpumped at a delay of 4 ps. In an unpumped diffraction pattern, the more intense of the two highlighted Bragg peaks results from scattering off the WSe₂ monolayer, the other from the MoSe₂ monolayer. The reverse is true of the pumped difference image inset to Fig. 2(a): the more intense peak results from the stronger response of the MoSe₂ layer. The interlayer twist angle controls the separation in reciprocal space between the two Bragg peaks, measured here to be 2°.

The sixfold symmetry of the real-space moiré pattern entails that scattering from the moiré superlattice forms a hexagon dressing each Bragg peak. The satellites observable in the inset to Fig. 2(a) lie at scattering vectors where monolayer contributions overlap. Static selected area electron diffraction (SAED) from twisted bilayer graphene performed by others shows that the intensity of moiré satellite peaks decays exponentially with twist angle between 0.5°–2° [10]. These results, and static SAED data from 1° twisted WSe₂/MoS₂ [48], are consistent with our observation of two satellites along the midline of a ($\bar{1}\bar{1}20$) Bragg pair. Interlayer interactions strain the monolayers: simulated diffraction patterns presented in Fig. 2(b) show that satellite peaks are absent without this strain and grow in intensity as strain increases (see Appendix D for simulation details). A future work will present time-series data showing the detailed dynamics of the moiré superstructure.

B. Reaching Poisson-limited experimental uncertainty

In this section, we demonstrate with experimental data how fast beam chopping coupled with high detector frame rate dramatically improves signal to noise in ultrafast pump–probe experiments. The chopping concept is illustrated in Fig. 3. To put the results of this section in context, it is necessary to briefly summarize the relevant sources of noise. The typical signal in UED is the fractional change in scattering intensity $\Delta I/I$ as a function of delay time and scattering angle. Distinguishing *pumped* exposures, when the pump beam is incident on the sample, from *unpumped* exposures, when the pump beam is off, $\Delta I/I$ can be expressed in terms of the ratio of the number N_s of scattered electrons within a given solid angle to

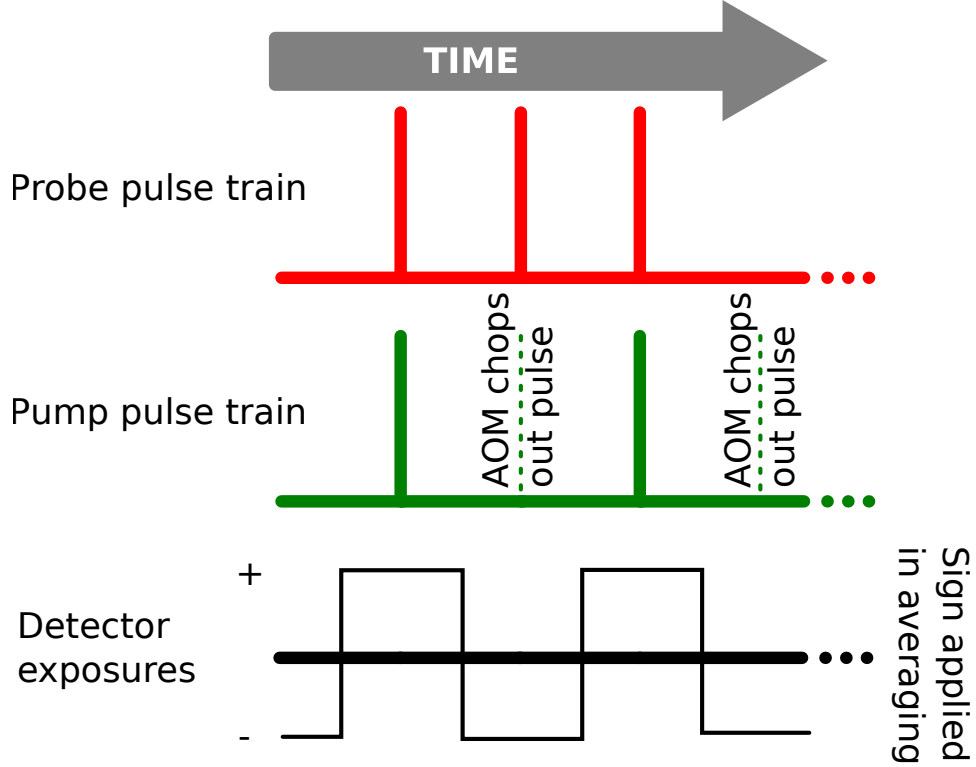


FIG. 3. Overview of beam chopping scheme: the probe pulses shown in red trigger an acousto-optic modulator (AOM, see Fig. 1) to block pump pulses, shown in green, from reaching the sample. Probe pulses synchronously trigger detector exposures, shown in black. Exposures enter the ensemble average with a positive sign if the pump gate is open, negative if the pump gate is blocked.

the number N_i of incident electrons:

$$\frac{\Delta I}{I} = \frac{(N_{sp}/N_{ip})}{(N_{su}/N_{iu})} - 1, \quad (1)$$

where the additional subscript p or u corresponds to the pumped or unpumped condition. The contribution of the probe beam to total experimental uncertainty σ_{total} in estimating $\Delta I/I$ is then analyzed by considering contributions from each N appearing in Eq. (1). These contributions are conveniently aggregated into four terms [49]:

$$\sigma_{\text{total}}^2 = \sigma_{\text{shot}}^2 + \sigma_{\text{detector}}^2 + \sigma_{\text{transport}}^2 + \sigma_{\text{source}}^2. \quad (2)$$

Each term in Eq. (2) corresponds to elements that together comprise the entire scattering experiment: σ_{shot} accounts for the Poisson distribution in the number of electron scattering

events; σ_{detector} accounts for uncertainty introduced in converting electron incidence into detector counts; finally, σ_{source} and $\sigma_{\text{transport}}$ account for uncertainty introduced in emitting and transporting electrons from source to detector. As the relative importance of each term depends on signal intensity [49], all four can be important in an experiment that aims to resolve diffraction features at separated intensity scales simultaneously.

The shot noise contribution σ_{shot} to $\Delta I/I$ is dominated by the contribution from scattered electrons, so that:

$$\sigma_{\text{shot}}^2 = \left(1 + \frac{\Delta I}{I}\right)^2 \left(\frac{1}{N_{sp}} + \frac{1}{N_{su}}\right). \quad (3)$$

As a numerical illustration, to resolve a 1% change in a diffraction feature intensity with 0.5% rms uncertainty requires a minimum of $\sim 10^5$ electrons scattered into that feature. The corresponding minimum accumulation time, supposing a high charge machine with 10^6 electrons per pulse at a 1 kHz repetition rate [22], and 10^{-3} scattering factor, is only 100 ms. Nonetheless, stroboscopic UED experiments often integrate for much longer to achieve this same level of experimental uncertainty (e.g., [22, 50, 51]), because in these experiments σ_{shot}^2 is not the most significant term in σ_{total}^2 .

Contributions to σ_{detector} depend on the detector technology, and include per count amplification noise as well as readout noise [49]. With respect to the EMPAD, rms read noise (where the average is taken over all pixels) is equivalent to 0.011 electrons at 140 keV, a signal-to-noise of 100. [52].

The final two terms in Eq. (2), $\sigma_{\text{transport}}$ and σ_{source} , are dominated by the contribution from incident electrons, which arises from loss of information about the incident beam. Significant loss of information occurs if the intensity of the beam at zero scattering angle is not recorded. Failure to record this information can occur because the beam at zero scattering angle saturates the dynamic range of the detector, but the EMPAD is not saturated in the micro-diffraction experiments we report here. Instead, in our high-momentum-resolution experiments at long camera length, e.g., the inset to Fig. 2(a), the 2 cm diameter of the 128×128 pixel detector does not allow simultaneous sampling of the zero-angle peak together with the diffraction features of interest — the sidebands due to moiré interlayer interactions. This limitation could be overcome by combining multiple detectors into a larger array, as has been demonstrated with a version of the EMPAD in x-ray imaging [31]. Jit-

ter and drift arising from electron transport are specific to the experimental setup and lab environment. With reference to our setup, a micron scale probe defining aperture in micro-diffraction mode makes the transmitted current sensitive (at the 0.1% – %1 level relevant in UED) to micro-radian changes in beam pointing. Kicks of this size are likely the result of integrating electromagnetic pollution (partially compensated by Helmholtz coils) along the 3 m distance from cathode to sample. Techniques to achieve electromagnetically, as well as mechanically, cleaner lab environments developed for atomic resolution scanning transmission microscopy could also be implemented to improve beam transport in micro-UED [53].

Absent direct measurements, the number of incident electrons must be estimated from correlated information, for example, monitored photo-emission laser power and acquisition time [49]. In our micro-diffraction experiment, these indirect sources of information cannot track fluctuations due to transport through our probe-defining aperture just upstream of the sample. Figure 4 shows a measured frequency spectrum of total current transmitted through our 10 μm probe-defining aperture.

To demonstrate that beam chopping eliminates jitter and drift as sources of uncertainty in pump-probe experiments, Fig. 5(a) shows the measurement of the ultrafast response at two chopping frequencies with the small probe beam. The trend is an exponential decay convolved with the instrument response [54]. The non-zero sample response at delay times earlier than the pump arrival is due to 1 kHz thermal cycling, investigated below. Each data point is acquired with a two-minute integration time. The spread in the data at the slow chopping rate (one minute pumped, followed by one minute unpumped) is comparable to the size of the ultrafast effect. In stark contrast, the data acquired at the 500 Hz chopping frequency follows the fitted trend closely.

Further investigating the dependence of experimental uncertainty on beam-chopping frequency, we benchmark our experimental uncertainty with pump-probe time-series data, summarized in Fig. 5(b). We can estimate frequency dependence by taking averages with the respect to an ensemble of time-bins of variable duration W . We compute a variance-to-mean ratio (VMR) as a function of W :

$$\text{VMR}(W) := \frac{\text{Var}_W(N_{sp} - N_{su})}{\text{E}_W[N_{sp} + N_{su}]}, \quad (4)$$

where $\text{Var}_W(X)$ denotes the variance of X over duration- W time-bins and $\text{E}_W[X]$ the mean

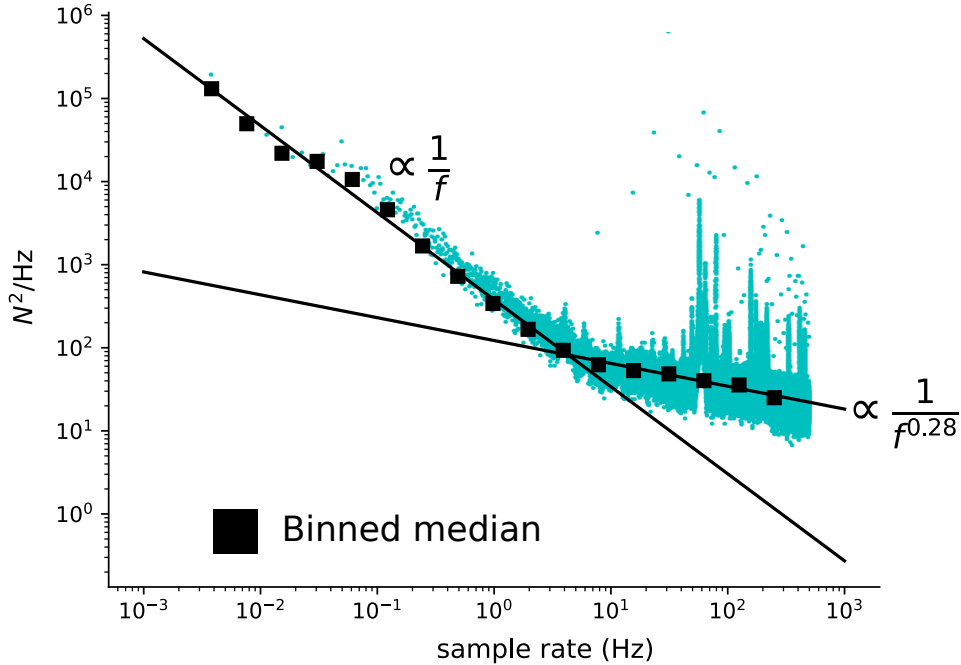


FIG. 4. Power spectral density (PSD) of the number of electrons transmitted through our $10 \mu\text{m}$ probe-defining aperture. Fluctuations in transmitted intensity are dominated by spatial drift of the beam on the probe-defining aperture. The PSD is computed from 90 min of time-series data using the Welch method. To fit the trend lines, the PSD is binned in exponentially spaced frequency intervals.

over the same bins. The VMR defined in Eq. (4) can be interpreted as the square of the experimental uncertainty in estimating the effect of pumping the sample, normalized by the shot noise limit. If N_{su}, N_{sp} are drawn from independent Poisson distributions then the VMR must equal one. The VMR rises above one with the introduction of fluctuations in the mean of the Poisson distribution, due, e.g., to fluctuating laser power on the photocathode, and $1/f$ noise in the steering magnets and accelerating voltage.

Figure 5(b) plots $\sqrt{\text{VMR}}$ (as defined in Eq. (4)) against chopping frequency and compares higher intensity Bragg scattering peaks with the 30% weaker superlattice peaks. The two data sets are fit to power law trend lines. Both data-sets are at the shot noise floor when chopped at 500 Hz. The data reveals that the higher the scattering rate, the higher the chopping frequency required to hit the shot noise floor (holding fixed the total integration

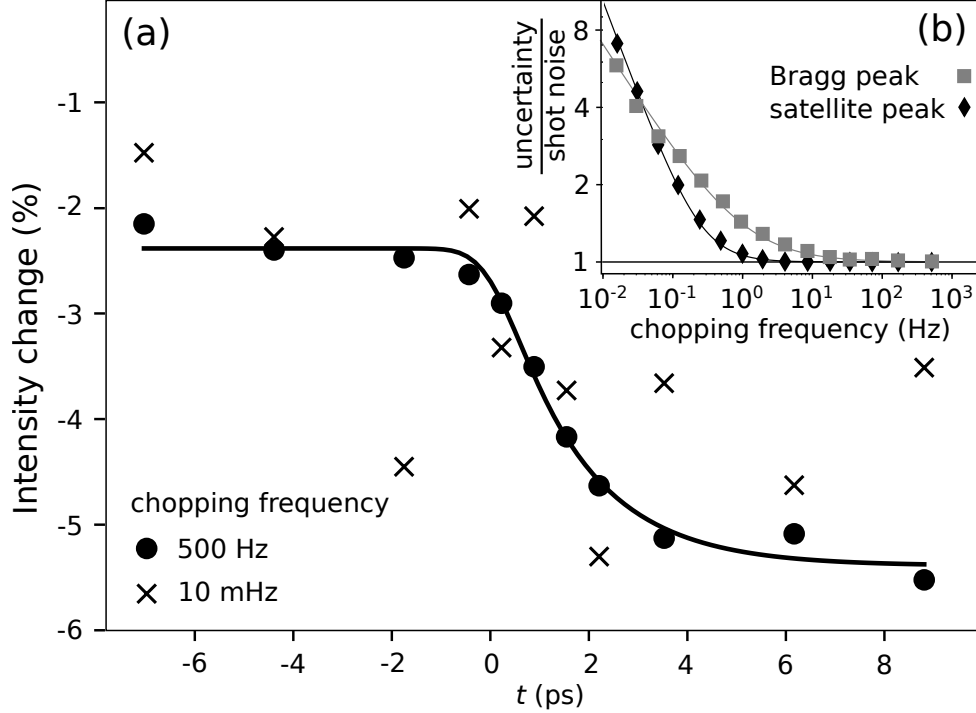


FIG. 5. (a) Measurement of the ultrafast Debye–Waller effect, summing peaks 1–4 in Fig. 2(a), comparing data quality with high and low chopping frequencies, each data point integrated for two minutes. (b) Measurement uncertainty as a function of chopping frequency: referring to the variance-to-mean ratio (VMR) defined in Eq. (4), the vertical axis shows $\sqrt{\text{VMR}}$ and can be interpreted as the ratio of total uncertainty to the shot noise limit set by the total integration time. Two curves compare different scattering rates: gray squares show a scattering rate equivalent to the Bragg peak labeled 1 in Fig. 2(a), black diamonds show a scattering rate equivalent to the satellite peak labeled 4 in Fig. 2(a).

time). At the higher scattering rate, the VMR is appreciably greater than unity at chopping frequencies below 100 Hz, while at the lower scattering rate, the VMR begins to rise above shot noise only below 10 Hz. The explanation is that more counts for fixed acquisition time reduces the Poisson contribution to the noise in any given frequency band, increasing the experimental sensitivity to jitter and drift in the same band. It follows that for fixed acquisition time the chopping frequency required to reach the shot noise floor depends both on the experimental setup – the average probe current – and on the intrinsic details of the scattering mechanism, e.g., low intensity thermal diffuse scattering is shot noise limited at a lower chopping frequency than high intensity Bragg scattering.

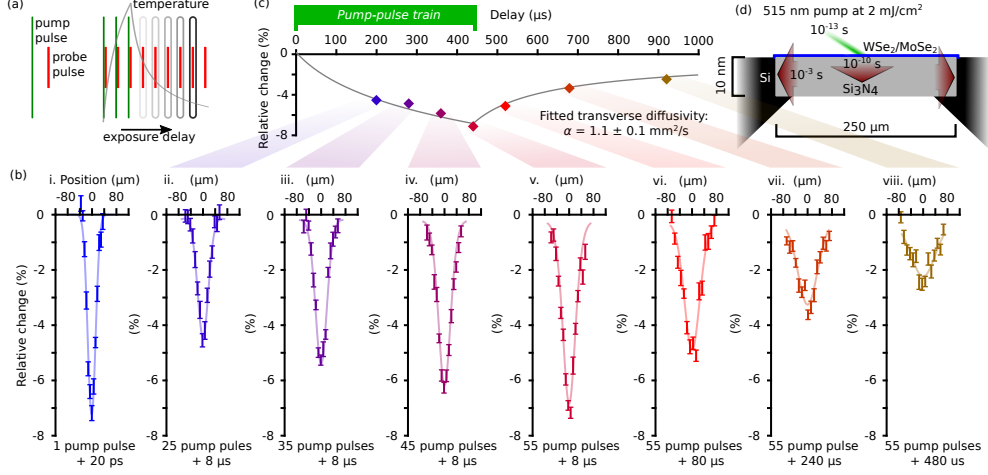


FIG. 6. Multi-dimensional, multi-scale sample thermometry. (a) Long-delay scanning technique: pump pulses are gated while microsecond exposures isolate individual probe pulses as they arrive at $8 \mu\text{s}$ intervals, sampling femtosecond pulses at delays up to a millisecond and longer. (b) i.–viii. Change in diffraction intensity $\Delta I/I$ (vertical axis) versus the spatial displacement of pump and probe (horizontal axis), at pump–probe delays spanning eight orders of magnitude. The diffraction signal is the sum of all electron counts in the highlighted region around the $(\bar{1}\bar{1}20)$ peak indicated in Fig. 2: both monolayers contribute. (b) i. The ultrafast response 20 ps after one pump pulse, with the solid line showing a Gaussian fit. (b) ii. The response $8 \mu\text{s}$ after a $200 \mu\text{s}$ pump-pulse train containing 25 pump pulses. (b) iii.–v. Extending the duration of the pump-pulse train to a maximum of $440 \mu\text{s}$, the response $8 \mu\text{s}$ after the final pulse in the train: the method is illustrated in Fig. 1. (b) vi.–viii. Sample relaxation, holding the $440 \mu\text{s}$ pump-pulse train duration fixed. (c) $\Delta I/I$ (vertical axis), at $0 \mu\text{m}$ spatial displacement, versus pump–probe delay. All solid lines in (b) ii.–viii. and (c) are cross sections of the fitted, three-parameter diffusion model summarized in Eq. (5). The fitted transverse diffusivity $\alpha = 1.1 \pm 0.1 \text{ mm}^2/\text{s}$. (d) Heat diffusion time-scales: the duration of pump excitation is 10^{-13} s , heat is transferred from bilayer to 10 nm thick substrate in 10^{-10} s , heat diffuses transversely to the sample boundaries over 10^{-3} s .

C. Scanning micro-diffraction in space and time

The ability to isolate and compare the response to fs excitation at μs and ms delays is critical to understanding microscopic heat transport and potentially the formation of metastable phases [18]. The pulse-picking method illustrated in Fig. 1 allows us to perform

multi-dimensional, multi-scale thermometry on $\text{WSe}_2/\text{MoSe}_2$ via the Debye–Waller effect. The detector frame rate sets the effective repetition rate of the pulse-picked probe, so that the kHz frame rate reduces the time required to perform the experiment from weeks with a conventional CCD to eight hours with the EMPAD.

Our multi-dimensional, multi-scale thermometry data is shown in Fig. 6. The three data dimensions are probe delay and probe position (both plotted horizontally) and the relative change in diffraction intensity $\Delta I/I$ (plotted vertically). Colors indicate which spatial cuts in Fig. 6(b) correspond to the pump–probe delay shown in Fig. 6(c). Panel (b) i. shows the ultrafast response taken at a pump delay of 20 ps. The remaining data are taken by progressively extending the duration of the pump pulse train and probing the sample 8 μs after the final pulse in the pump pulse train. The 8 μs increment corresponds to the period between pulses at our 125 kHz repetition rate. The data in Fig. 6(b) ii.–v. clearly show the accumulation of energy through the duration of the pump pulse train, while panels vi.–viii. show the dissipation of energy to the sample boundaries after the pump-pulse train terminates.

In the limit that the relaxed sample temperature is well above zero and the temperature change ΔT is small, both compared to the sample Debye temperature, the fractional change in the Bragg scattering rate $\Delta I/I$ with scattering vector \mathbf{k} is proportional to $k^2 \Delta T$. Hence, by scanning $\Delta I/I$ as a function of pump spatial position and pump delay, it is possible to map out thermal transport in the sample. We choose a low pump fluence of 2 mJ/cm^2 as a compromise between, on the one hand, maintaining linearity in the relationship between $\Delta I/I$ and T , and on the other, minimizing Poisson noise in the diffraction difference.

To model the heat transport phenomenology, we fit to our diffraction signal $\Delta I/I \propto T$ to an analytic, approximate solution to the inhomogeneous 2D heat equation,

$$\left[\frac{\partial}{\partial t} - \alpha \nabla^2 \right] T(t, \mathbf{x}; \alpha, A, \sigma_0) = f(t, \mathbf{x}; A, \sigma_0). \quad (5)$$

The periodic solution $T(t, \mathbf{x}; \alpha, A, \sigma_0)$ contains three parameters: the diffusion constant α , and the amplitude A and width σ_0 of the pump pulses. The forcing term $f(t, \mathbf{x}; A, \sigma_0)$ represents the pump injecting energy into the system. The model makes no assumptions concerning the transport mechanism. The diffraction intensity I is the sum of peaks labeled

1–4 in Fig. 2(a). Eq. (5) is solvable by Fourier series, and we obtain an analytic approximation by simply truncating this series to finite order. The Supplemental Material provides a detailed derivation of the explicit expression.

We find excellent agreement between our data and three-parameter phenomenological model. Solid lines in Fig. 6(b) ii–viii show the spatial profile implied by the fitted model; the solid line in Fig. 6(c) shows the fitted temperature envelope at the center of the sample square. The interpretation of Fig. 6 is that the extreme aspect ratio of the bilayer–substrate combination – 10 nm thick versus 250 μm wide – results in two relaxation timescales: a fast timescale, $\tau_{\text{fast}} < 1$ ns, and a slow timescale, $\tau_{\text{slow}} > 1$ ms. The fit implies a decay in the temperature of the bilayer following the arrival of the first pump pulse to 5% of its peak value before the arrival of the second. This 5% residue accumulates for the duration of the 440 μs pulse train and, following the end of the pulse train, relaxes exponentially at a rate set by the sample window size L : $\tau_{\text{slow}} = L^2/(2\pi^2\alpha)$.

The fit in Fig. 6 gives the value $\tau_{\text{slow}} = 3$ ms. When, as in our experiment, the period between pump pulse trains is less than the relaxation time, the bilayer reaches a periodic state in which the minimum temperature of the pumped region during a cycle remains elevated above the temperature of the boundaries. The estimate of τ_{slow} unambiguously defines the repetition rate that allows for the sample to fully relax before the arrival of each pump pulse in stroboscopic data acquisition. This relaxation time is sample and substrate dependent, as are the physical implications of pumping at a repetition rate faster than sample relaxation. Our method of extending the range of ultrafast pump–probe delays to μs –ms enables us to investigate these issues experimentally.

Pump–probe delays in the μs –ms range provide a technique to extract the transverse thermal conductivity of the bilayer. This intrinsic property cannot be inferred from sub-ns data alone, because the ultrafast relaxation we observe is dominated by the interfacial resistance between bilayer and SiN substrate, as heat is transferred across the nm dimension [22]. Whereas, on the slow timescale, the bilayer and SiN substrate provide parallel channels for conducting heat transversely over the 10^{-4} m distance to the Si wafer at the transverse boundary.

The transverse diffusivity parameter α that we fit with our phenomenological 2D model (solid lines in Fig. 6(b)–(c)) does not discriminate between bilayer and substrate contributions.

From the same data, finite-element simulations (see, e.g., [55]) can extract the intrinsic transverse diffusivity of the bilayer. We find close agreement between simulation and the approximate analytic relationship,

$$\alpha_{\text{BL}} = \alpha_{\text{exp}} + \frac{C_{\text{SiN}}}{C_{\text{BL}}}(\alpha_{\text{exp}} - \alpha_{\text{SiN}}), \quad (6)$$

where α_{BL} , C_{BL} are the transverse diffusivity and heat capacity of the bilayer, α_{SiN} , C_{SiN} are the transverse diffusivity and heat capacity of the substrate, and α_{exp} is the transverse diffusivity of the bilayer–substrate combination that we measure experimentally.

Hypothetically, data obtained from a freestanding bilayer would be simpler to analyze: however, an implication of the data we collect is that pumping a freestanding bilayer with 2 mJ/cm² fluence at 10² Hz or faster repetition rates would cause irreversible damage within a few pulses, without the SiN present to act as a heatsink. In testing samples mounted on SiN, we observed an irreversible drop in scattering intensity at a fluence of 3 mJ/cm². A scanning-micrograph recorded with our electron probe showed the damage to be localized to the region illuminated by the pump-laser spot, a conclusion confirmed by post-mortem optical microscope images of the sample. The ability to reach higher fluences reversibly is important because even reversible structural responses can change discontinuously as a function of fluence [6], possibly because the out-of-equilibrium electron population excited by the pump undergoes a phase transition as a function of the density of excited charges — in the case of our sample from an excitonic to a free electron gas [43]. These fluence-dependent physical mechanisms cannot be fully explored in experiments where fluence is constrained by the sample environment.

III. DISCUSSION AND CONCLUSION

This work has presented new, dramatic advantages of an integrating direct electron detector with high dynamic range and fast frame rate for structural dynamics data acquisition. We are able to resolve the ultrafast response of a 10 nm periodic moiré superlattice, and to track the ms long thermal relaxation of the WSe₂/MoSe₂ bilayer following ultrafast excitation. Future experiments plan to apply this technique to investigate the effects of interlayer interactions on thermal transport in two ways: by measuring the dependence of transverse relaxation on bilayer twist angle [43], and by tuning pump photon energy to resonantly excite a specific

monolayer in the heterostructure.

Our results show that beam chopping at frequencies up to 500 Hz eliminates experimental uncertainties that are caused by non-Poissonian fluctuations in the probe current on target. In micro-diffraction, an important non-Poissonian source of uncertainty is positioning error on the probe defining aperture. Beam chopping is especially important in experiments where detector saturation or limits on field of view (at fine angular resolution) preclude measuring the total charge on target per pulse. Beam chopping is a complement to techniques that eliminate time-of-arrival jitter as a source of experimental uncertainty [56].

The next generation EMPAD increases the frame rate to 10 kHz [47], which raises the maximum chopping frequency. Our results suggest that chopping frequencies above 1 kHz, while unnecessary for our system in micro-diffraction mode (100 electrons on target per pulse) have the potential to significantly improve signal-to-noise in experiments that involve large bunch charges of 10^5 electrons or more, and in high-flux x-ray experiments with free electron laser sources.

A natural extension of our pulse-picking technique is to utilize a commercially available femtosecond GHz oscillator and fast pulse picker to achieve nanosecond pulse selection precision prior to the amplification stage. Such a system, when coupled with a delay stage to cover the range < 1 ns, would provide seamless delay capability from femtoseconds to seconds with femtosecond resolution. Measuring the transverse relaxation time of the bilayer, we demonstrate an experimental method for unambiguously defining the sample-dependent optimal repetition-rate for ultrafast stroboscopic data collection. Our results highlight the need for pump-probe modalities that can access multiple time and intensity scales when investigating the rich, multi-scale physics of 2D quantum materials.

This work was supported by the U.S Department of Energy, awards DE-SC0020144 and DE-SC0017631, and U.S. National Science Foundation Grant PHY-1549132, the Center for Bright Beams. D.L., A.S., and A.M.L. acknowledge support from the U.S. Department of Energy, Office of Science, Basic Energy Sciences, Materials Sciences and Engineering Division, under Contract DE-AC02-76SF00515.

Appendix A: MUltrafast Electron Diffraction

Our beamline is shown in Fig. 7(a). The probe electron beam is photoemitted with 650 nm laser pulses and accelerated to a primary energy of 140 keV, and the sample is pumped with 515 nm pulses obtained from the same 1030 nm source. Electron beam optics for magnifying the diffraction pattern are shown in Fig. 7(b). Our scanning ultrafast electron diffraction technique is illustrated in Fig. 1. The spot size of the electron probe on the sample is defined by a laser-milled aperture 15 mm upstream. An in-vacuum lens focuses the 515 nm pump pulse to a 10 μm rms spot on the sample, and the pump spot is steered on the sample by an out-of-vacuum mirror. A virtual-sample camera placed out of vacuum monitors the location of the central peak of the pump laser to μm precision. The duty cycle of the acousto-optic modulator that gates pump pulses is variable to single-pulse precision: we typically choose a duty-cycle to match the detector exposure, eliminating un-detected pulses and thus reducing the thermal load on the sample. We verify the reliability of the timing system by measuring the total pump-energy per exposure with the detector, and we see a sharp quantization of energy as a function of exposure length at intervals of the 8 μs laser repetition period. Pump and probe beams are aligned by performing knife-edge scans at the vertical and horizontal sample edges. For the data presented in main text Fig. 6, knife-edge scans give 6 μm rms probe size in the sample plane.

Appendix B: Detector Saturation

We observe saturation at 60 incident electrons per pixel per pulse in pulsed operation at 140 keV. We arrive at this experimental estimate by averaging single shot measurements, and controlling the charge per pulse by varying the charge transmitted through the probe-defining aperture. The maximum charge that the EMPAD can remove per charge-removal cycle per pixel is equivalent to 11 incident electrons at this beam energy. The maximum is set by protection diodes that limit the peak charging current of each pixel's storage capacitor. There thus appears to be a discrepancy between, on the one hand, the saturation threshold we observe and, on the other, the limit set by the electronics. A plausible resolution of the discrepancy is this: the high charge density in pulsed operation results in the creation of an electron-hole plasma with microseconds lifetime. The long-lived plasma is removed

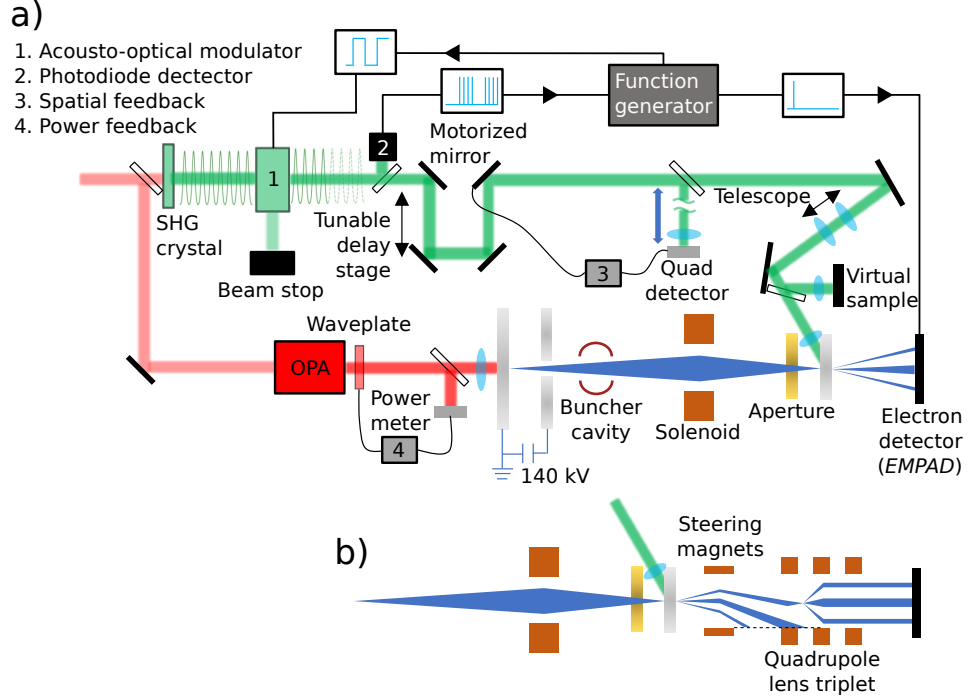


FIG. 7. (a) Schematic of the UED beamline, see Ref. [39] for details: a 1030 nm Yb-fiber laser drives an optical parametric amplifier that sends 650 nm light pulses to the photocathode. Photoemitted bunches are accelerated to 140 keV, compressed by an rf cavity, collimated by a probe-defining aperture, and are collected by the detector after scattering on the sample; the same 1030 nm pulses are split and frequency doubled to synchronously pump the sample. (b) Modification of the detector section of the beamline to accommodate a magnetic quadrupole electron lens triplet. The lens triplet enables angular magnification of the scattering pattern. A diffraction feature is selected for magnification on the detector with a steering magnet upstream of the lens triplet.

over multiple charge-removal cycles [57]. The charge-removal circuitry cycles at 2 MHz, the probe beam repetition rate is 125 kHz, and hence there are 16 charge removal cycles for every probe pulse.

Appendix C: Sample Preparation

MoSe₂ and WSe₂ monolayers are exfoliated from bulk MoSe₂ and WSe₂ single crystals (HQ graphene) onto 285 nm SiO₂/Si substrate sequentially using a gold tape exfoliation technique [12], forming heterostructures with lateral dimensions of mm scale. The crystal

orientations of the monolayers in the heterostructure are aligned with the crystal edges, and further confirmed in electron diffraction. The heterostructures are later transferred onto 10 nm thick, $250 \mu\text{m} \times 250 \mu\text{m}$ Si_3N_4 windows on TEM grids (SiMPore), using a wedging transfer technique with cellulose acetate butyrate (CAB) polymer [58].

Appendix D: Diffraction simulation

Diffraction patterns in Fig. 2(b) are computed from the Fourier transform of the real-space phenomenological model presented in [59]. Retaining only the longest-wavelength components of the PLD, atomic positions are displaced by a spatially varying vector field $\mathbf{u}(\mathbf{x})$ with explicit expression,

$$\mathbf{u}(\mathbf{x}) = \frac{\epsilon}{\|\mathbf{k}_0\|} \left(\hat{\mathbf{y}} \frac{\partial}{\partial x} - \hat{\mathbf{x}} \frac{\partial}{\partial y} \right) \left(\cos(\mathbf{k}_0 \cdot \mathbf{x}) + \cos(\mathbf{k}_1 \cdot \mathbf{x}) + \cos([\mathbf{k}_0 - \mathbf{k}_1] \cdot \mathbf{x}) \right) \quad (\text{D.1})$$

where ϵ is the amplitude parameter and \mathbf{k}_i are the reciprocal lattice vectors of the moiré superlattice.

-
- [1] H. Ihee, V. A. Lobastov, U. M. Gomez, B. M. Goodson, R. Srinivasan, C.-Y. Ruan, and A. H. Zewail, Direct imaging of transient molecular structures with ultrafast diffraction, *Science* **291**, 458 (2001).
 - [2] A. Cavalleri, C. Tóth, C. W. Siders, J. A. Squier, F. Ráksi, P. Forget, and J. C. Kieffer, Femtosecond structural dynamics in VO_2 during an ultrafast solid-solid phase transition, *Phys. Rev. Lett.* **87** (2001).
 - [3] B. J. Siwick, J. R. Dwyer, R. E. Jordan, and R. J. D. Miller, An atomic-level view of melting using femtosecond electron diffraction, *Science* **302**, 1382 (2003).
 - [4] N. Gedik, D.-S. Yang, G. Logvenov, I. Bozovic, and A. H. Zewail, Nonequilibrium phase transitions in cuprates observed by ultrafast electron crystallography, *Science* **316**, 425 (2007).

- [5] L. Stojchevska, I. Vaskivskiy, T. Mertelj, P. Kusar, D. Svetin, S. Brazovskii, and D. Mihailovic, Ultrafast switching to a stable hidden quantum state in an electronic crystal, *Science* **344**, 177 (2014).
- [6] E. J. Sie, C. M. Nyby, C. D. Pemmaraju, S. J. Park, X. Shen, J. Yang, M. C. Hoffmann, B. K. Ofori-Okai, R. Li, A. H. Reid, S. Weathersby, E. Mannebach, N. Finney, D. Rhodes, D. Chenet, A. Antony, L. Balicas, J. Hone, T. P. Devereaux, T. F. Heinz, X. Wang, and A. M. Lindenberg, An ultrafast symmetry switch in a Weyl semimetal, *Nature* **565**, 61 (2019).
- [7] C. Broholm, I. Fisher, J. Moore, M. Murnane, A. Moreo, J. Tranquada, D. Basov, J. Freericks, M. Aronson, A. MacDonald, E. Fradkin, A. Yacoby, N. Samarth, S. Stemmer, L. Horton, J. Horwitz, J. Davenport, M. Graf, J. Krause, M. Pechan, K. Perry, J. Rhyne, A. Schwartz, T. Thiyagarajan, L. Yarris, and K. Runkles, Basic research needs workshop on quantum materials for energy relevant technology, USDOE Off. Sci. (2016).
- [8] G. Carini, P. Denes, S. Gruener, and E. Lessner, Neutron and X-ray detectors, USDOE Off. Sci. (2012).
- [9] Y. Cao, V. Fatemi, S. Fang, K. Watanabe, T. Taniguchi, E. Kaxiras, and P. Jarillo-Herrero, Unconventional superconductivity in magic-angle graphene superlattices, *Nature* **556**, 43 (2018).
- [10] H. Yoo, R. Engelke, S. Carr, S. Fang, K. Zhang, P. Cazeaux, S. H. Sung, R. Hovden, A. W. Tsun, T. Taniguchi, K. Watanabe, G.-C. Yi, M. Kim, M. Luskin, E. B. Tadmor, E. Kaxiras, and P. Kim, Atomic and electronic reconstruction at the van der Waals interface in twisted bilayer graphene, *Nat. Mater.* **18**, 448 (2019).
- [11] M. Liao, Z. Wei, L. Du, Q. Wang, J. Tang, H. Yu, F. Wu, J. Zhao, X. Xu, B. Han, K. Liu, P. Gao, T. Polcar, Z. Sun, D. Shi, R. Yang, and G. Zhang, Precise control of the interlayer twist angle in large scale MoS₂ homostructures, *Nat. Commun.* **11**, 2153 (2020).
- [12] F. Liu, W. Wu, Y. Bai, S. H. Chae, Q. Li, J. Wang, J. Hone, and X.-Y. Zhu, Disassembling 2D van der Waals crystals into macroscopic monolayers and reassembling into artificial lattices, *Science* **367**, 903 (2020).
- [13] S. E. Kim, F. Mujid, A. Rai, F. Eriksson, J. Suh, P. Poddar, A. Ray, C. Park, E. Fransson, Y. Zhong, D. A. Muller, P. Erhart, D. G. Cahill, and J. Park, Extremely anisotropic van der Waals thermal conductors, *Nature* **597**, 660 (2021).

- [14] B. Zhao, Z. Wan, Y. Liu, J. Xu, X. Yang, D. Shen, Z. Zhang, C. Guo, Q. Qian, J. Li, R. Wu, Z. Lin, X. Yan, B. Li, Z. Zhang, H. Ma, B. Li, X. Chen, Y. Qiao, I. Shakir, Z. Almutairi, F. Wei, Y. Zhang, X. Pan, Y. Huang, Y. Ping, X. Duan, and X. Duan, High-order superlattices by rolling up van der Waals heterostructures, *Nature* **591**, 385 (2021).
- [15] A. C. Gadelha, D. A. A. Ohlberg, C. Rabelo, E. G. S. Neto, T. L. Vasconcelos, J. L. Campos, J. S. Lemos, V. Ornelas, D. Miranda, R. Nadas, F. C. Santana, K. Watanabe, T. Taniguchi, B. van Troeye, M. Lamparski, V. Meunier, V.-H. Nguyen, D. Paszko, J.-C. Charlier, L. C. Campos, L. G. Cançado, G. Medeiros-Ribeiro, and A. Jorio, Localization of lattice dynamics in low-angle twisted bilayer graphene, *Nature* **590**, 405 (2021).
- [16] D. Basov, R. Averitt, and D. Hsieh, Towards properties on demand in quantum materials, *Nat. Mater.* **16**, 1077 (2017).
- [17] E. Y. Andrei, D. K. Efetov, P. Jarillo-Herrero, A. H. MacDonald, K. F. Mak, T. Senthil, E. Tutuc, A. Yazdani, and A. F. Young, The marvels of moiré materials, *Nat. Rev. Mater.* **6**, 201 (2021).
- [18] D. Fausti, R. I. Tobey, N. Dean, S. Kaiser, A. Dienst, M. C. Hoffmann, S. Pyon, T. Takayama, H. Takagi, and A. Cavalleri, Light-induced superconductivity in a stripe-ordered cuprate, *Science* **331**, 189 (2011).
- [19] S. Weathersby, G. Brown, M. Centurion, T. Chase, R. Coffee, J. Corbett, J. Eichner, J. Frisch, A. Fry, M. Gühr, *et al.*, Mega-electron-volt ultrafast electron diffraction at SLAC national accelerator laboratory, *Rev. Sci. Instrum.* **86** (2015).
- [20] A. Feist, N. Bach, N. R. da Silva, T. Danz, M. Möller, K. E. Priebe, T. Domröse, J. G. Gatzmann, S. Rost, J. Schauss, *et al.*, Ultrafast transmission electron microscopy using a laser-driven field emitter: Femtosecond resolution with a high coherence electron beam, *Ultramicroscopy* **176**, 63 (2017).
- [21] J. Li, J. Lu, A. Chew, S. Han, J. Li, Y. Wu, H. Wang, S. Ghimire, and Z. Chang, Attosecond science based on high harmonic generation from gases and solids, *Nat. Commun.* **11** (2020).
- [22] T. L. Britt, Q. Li, L. P. René de Cotret, N. Olsen, M. Otto, S. A. Hassan, M. Zacharias, F. Caruso, X. Zhu, and B. J. Siwick, Direct view of phonon dynamics in atomically thin MoS₂, *Nano Lett.* (2022).
- [23] R. R. Meyer and A. Kirkland, The effects of electron and photon scattering on signal and noise transfer properties of scintillators in CCD cameras used for electron detection, *Ultra-*

- microscopy **75**, 23 (1998).
- [24] G. Y. Fan and M. H. Ellisman, Digital imaging in transmission electron microscopy, *J. Microsc.* **200**, 1 (2000).
- [25] J. M. Zuo, Electron detection characteristics of a slow-scan CCD camera, imaging plates and film, and electron image restoration, *Microsc. Res. Tech.* **49**, 245 (2000).
- [26] S. M. Gruner, M. W. Tate, and E. F. Eikenberry, Charge-coupled device area x-ray detectors, *Rev. Sci. Instrum.* **73**, 2815 (2002).
- [27] R. S. Ruskin, Z. Yu, and N. Grigorieff, Quantitative characterization of electron detectors for transmission electron microscopy, *J. Struct. Biol.* **184**, 385 (2013).
- [28] T. Vecchione, P. Denes, R. K. Jobe, I. J. Johnson, J. M. Joseph, R. K. Li, A. Perazzo, X. Shen, X. J. Wang, S. P. Weathersby, J. Yang, and D. Zhang, A direct electron detector for time-resolved MeV electron microscopy, *Rev. Sci. Instrum.* **88** (2017).
- [29] A. Allahgholi, J. Becker, A. Delfs, R. Dinapoli, P. Göttlicher, H. Graafsma, D. Greiffenberg, H. Hirsemann, S. Jack, A. Klyuev, H. Krüger, M. Kuhn, T. Laurus, A. Marras, D. Mezza, A. Mozzanica, J. Poehlsen, O. Shefer Shalev, I. Sheviakov, B. Schmitt, J. Schwandt, X. Shi, S. Smoljanin, U. Trunk, J. Zhang, and M. Zimmer, Megapixels @ Megahertz – The AGIPD high-speed cameras for the European XFEL, *Nucl. Instrum.* **942** (2019).
- [30] F. Leonarski, S. Redford, A. Mozzanica, C. Lopez-Cuenca, E. Panepucci, K. Nass, D. Ozerov, L. Vera, V. Olieric, D. Buntschu, R. Schneider, G. Tinti, E. Froejdh, K. Diederichs, O. Bunk, B. Schmitt, and M. Wang, Fast and accurate data collection for macromolecular crystallography using the jungfrau detector, *Nat. Mater.et* **15**, 799 (2018).
- [31] M. W. Tate, D. Chamberlain, K. S. Green, H. T. Philipp, P. Purohit, C. Strohman, and S. M. Gruner, A medium-format, mixed-mode pixel array detector for Kilohertz X-ray imaging, *J. Phys. Conf. Ser.* **425** (2013).
- [32] Y. Jiang, Z. Chen, Y. Han, P. Deb, H. Gao, S. Xie, P. Purohit, M. W. Tate, J. Park, S. M. Gruner, V. Elser, and D. A. Muller, Electron ptychography of 2D materials to deep sub-ångström resolution, *Nature* **559**, 343 (2018).
- [33] Z. Chen, Y. Jiang, Y.-T. Shao, M. E. Holtz, M. Odstril, M. Guizar-Sicairos, I. Hanke, S. Ganschow, D. G. Schlom, and D. A. Muller, Electron ptychography achieves atomic-resolution limits set by lattice vibrations, *Science* **372**, 826 (2021).

- [34] J. L. Hart, A. C. Lang, A. C. Leff, P. Longo, C. Trevor, R. D. Twesten, and M. L. Taheri, Direct detection electron energy-loss spectroscopy: a method to push the limits of resolution and sensitivity, *Sci. Rep.* **7**, 1 (2017).
- [35] P. S. Shen, The 2017 Nobel Prize in Chemistry: cryo- EM comes of age, *Anal. Bioanal. Chem.* **410**, 2053 (2018).
- [36] A. Faruqi and R. Henderson, Electronic detectors for electron microscopy, *Curr. Opin. Struct. Biol.* **17**, 549 (2007).
- [37] Y. M. Lee, Y. J. Kim, Y.-J. Kim, and O.-H. Kwon, Ultrafast electron microscopy integrated with a direct electron detection camera, *Struct. Dyn.* **4** (2017).
- [38] M. W. Tate, P. Purohit, D. Chamberlain, K. X. Nguyen, R. Hovden, C. S. Chang, P. Deb, E. Turgut, J. T. Heron, D. G. Schlom, *et al.*, High dynamic range pixel array detector for scanning transmission electron microscopy, *Microsc. Microanal.* **22**, 237 (2016).
- [39] W. H. Li, C. J. R. Duncan, M. B. Andorf, A. C. Bartnik, E. Bianco, L. Cultrera, A. Galdi, M. Gordon, M. Kaemingk, C. A. Pennington, L. F. Kourkoutis, I. V. Bazarov, and J. M. Maxson, A kiloelectron-volt ultrafast electron micro-diffraction apparatus using low emittance semiconductor photocathodes, *Struct. Dyn.* **9** (2022).
- [40] X. Shen, R. Li, U. Lundström, T. Lane, A. Reid, S. Weathersby, and X. Wang, Femtosecond mega-electron-volt electron microdiffraction, *Ultramicroscopy* **184**, 172 (2018).
- [41] C. Schrieffer, S. Lochbrunner, E. Riedle, and D. Nesbitt, Ultrasensitive ultraviolet-visible 20 fs absorption spectroscopy of low vapor pressure molecules in the gas phase, *Rev. Sci. Instrum.* **79** (2008).
- [42] Y. Bai, L. Zhou, J. Wang, W. Wu, L. J. McGilly, D. Halbertal, C. F. B. Lo, F. Liu, J. Ardelean, P. Rivera, N. R. Finney, X.-C. Yang, D. N. Basov, W. Yao, X. Xu, J. Hone, A. N. Pasupathy, and X.-Y. Zhu, Excitons in strain-induced one-dimensional moiré potentials at transition metal dichalcogenide heterojunctions, *Nat. Mater.* **19**, 1068 (2020).
- [43] J. Wang, Q. Shi, E.-M. Shih, L. Zhou, W. Wu, Y. Bai, D. Rhodes, K. Barmak, J. Hone, C. R. Dean, and X.-Y. Zhu, Diffusivity reveals three distinct phases of interlayer excitons in MoSe₂/WSe₂ heterobilayers, *Phys. Rev. Lett.* **126** (2021).
- [44] M. Adrian, A. Senftleben, S. Morgenstern, and T. Baumert, Complete analysis of a transmission electron diffraction pattern of a MoS₂-graphite heterostructure, *Ultramicroscopy* **166**, 9 (2016).

- [45] M. Domke, S. Rapp, M. Schmidt, and H. P. Huber, Ultrafast pump-probe microscopy with high temporal dynamic range, *Opt. Express* **20**, 10330 (2012).
- [46] A. S. Disa, M. Fechner, T. F. Nova, B. Liu, M. Först, D. Prabhakaran, P. G. Radaelli, and A. Cavalleri, Polarizing an antiferromagnet by optical engineering of the crystal field, *Nat. Phys.* **16**, 937 (2020).
- [47] H. T. Philipp, M. W. Tate, K. S. Shanks, L. Mele, M. Peemen, P. Dona, R. Hartong, G. van Veen, Y.-T. Shao, Z. Chen, *et al.*, Very-high dynamic range, 10,000 frames/second pixel array detector for electron microscopy, *Microsc. Microanal.* **28**, 425 (2022).
- [48] J. Kim, E. Ko, J. Jo, M. Kim, H. Yoo, Y.-W. Son, and H. Cheong, Anomalous optical excitations from arrays of whirlpooled lattice distortions in moiré superlattices, *Nat. Mater.* (2022).
- [49] C. Kealhofer, S. Lahme, T. Urban, and P. Baum, Signal-to-noise in femtosecond electron diffraction, *Ultramicroscopy* **159**, 19 (2015).
- [50] T. Chase, M. Trigo, A. Reid, R. Li, T. Vecchione, X. Shen, S. Weathersby, R. Coffee, N. Hartmann, D. Reis, *et al.*, Ultrafast electron diffraction from non-equilibrium phonons in femtosecond laser heated au films, *Appl. Phys. Lett.* **108** (2016).
- [51] J. Yang, X. Zhu, J. P. F. Nunes, J. K. Yu, R. M. Parrish, T. J. Wolf, M. Centurion, M. Gühr, R. Li, Y. Liu, *et al.*, Simultaneous observation of nuclear and electronic dynamics by ultrafast electron diffraction, *Science* **368**, 885 (2020).
- [52] J. T. Weiss, K. S. Shanks, H. T. Philipp, J. Becker, D. Chamberlain, P. Purohit, M. W. Tate, and S. M. Gruner, High dynamic range x-ray detector pixel architectures utilizing charge removal, *IEEE Trans. Nucl. Sci.* **64**, 1101 (2017).
- [53] D. A. Muller, E. J. Kirkland, M. G. Thomas, J. L. Grazul, L. Fitting, and M. Weyland, Room design for high-performance electron microscopy, *Ultramicroscopy* **106**, 1033 (2006).
- [54] R. P. Chatelain, V. R. Morrison, B. L. M. Klarenaar, and B. J. Siwick, Coherent and incoherent electron-phonon coupling in graphite observed with radio-frequency compressed ultrafast electron diffraction, *Phys. Rev. Lett.* **113** (2014).
- [55] P. Zalden, F. Quirin, M. Schumacher, J. Siegel, S. Wei, A. Koc, M. Nicoul, M. Trigo, P. Andreasson, H. Enquist, M. J. Shu, T. Pardini, M. Chollet, D. Zhu, H. Lemke, I. Ronneberger, J. Larsson, A. M. Lindenberg, H. E. Fischer, S. Hau-Riege, D. A. Reis, R. Mazzarello, M. Wuttig, and K. Sokolowski-Tinten, Femtosecond x-ray diffraction reveals a liquid – liquid phase

- transition in phase-change materials, *Science* **364**, 1062 (2019).
- [56] M. R. Otto, L. René de Cotret, M. J. Stern, and B. J. Siwick, Solving the jitter problem in microwave compressed ultrafast electron diffraction instruments: Robust sub-50 fs cavity-laser phase stabilization, *Struct. Dyn.* **4** (2017).
- [57] J. T. Weiss, J. Becker, K. S. Shanks, H. T. Philipp, M. W. Tate, and S. M. Gruner, Potential beneficial effects of electron-hole plasmas created in silicon sensors by XFEL-like high intensity pulses for detector development, *AIP Conf. Proc.* **1741** (2016).
- [58] G. F. Schneider, V. E. Calado, H. Zandbergen, L. M. K. Vandersypen, and C. Dekker, Wedging transfer of nanostructures, *Nano Lett.* **10**, 1912 (2010).
- [59] K. Zhang and E. B. Tadmor, Structural and electron diffraction scaling of twisted graphene bilayers, *J. Mech. Phys. Solids* **112**, 225 (2018).

Supplemental Material: Multi-scale time-resolved electron diffraction: a case study in moiré materials

C. J. R. Duncan, M. Kaemingk, W. H. Li, M. B. Andorf,
A. C. Bartnik, A. Galdi, M. Gordon, C. A. Pennington,
I. V. Bazarov, H. J. Zeng, F. Liu,
D. Luo, A. Sood, A. M. Lindenberg, M. W. Tate,
D. A. Muller, J. Thom-Levy, S. M. Gruner, J. M. Maxson

Diffusion Model

In this supplement we derive an explicit expression for the function used to fit the data in Fig. 5 of the main text.

Our model assumes: i. a square domain having side-length $L = 250 \mu\text{m}$, ii. that pump pulses strike the center of the square, and iii. that the boundaries of the square are held at constant temperature. We experimentally verify i. With respect to assumption ii., in experiment, we hold the probe spot fixed at the center of the sample window and scan the pump, as shown in Fig. 1 of the main text. Finally, assumption iii. is highly plausible given the overwhelming thermal mass of the Si wafer in which the SiN-supported sample window is embedded.

The fit function $T(x, y, t; \alpha, A, \sigma_0)$ with fit parameters α, A, σ_0 is a solution to the inhomogeneous heat equation:

$$\frac{\partial T}{\partial t} - \alpha \left[\frac{\partial^2 T}{\partial x^2} + \frac{\partial^2 T}{\partial y^2} \right] = f(x, y, t; A, \sigma_0). \quad (\text{S1})$$

Equation (S1) is subject to the condition that $T \equiv 0$ on a square boundary of side length L . The origin of the Cartesian coordinate system x, y lies at the center of the square. To avoid confusion, α is a fit parameter and no assumption is made in the fit as to the mechanism for heat diffusion.

We model the forcing term f in Eq. (S1) as a sequence of delta-function impulses, each having the same Gaussian spatial profile centered at the origin, with amplitude A and r.m.s size σ_0 . Pulses arrive in trains. Trains arrive at the rate ν and, within each train, pulses

arrive at the rate R . Each train contains J pulses. The explicit expression for f is then,

$$f(x, y, t; A, \sigma_0) = \frac{4A}{L^2} \sum_{q=-\infty}^{\infty} \sum_{j=0}^{J-1} \sum_{m=0}^{M-1} \sum_{n=0}^{N-1} \cos\left((2m+1)\frac{\pi x}{L}\right) \cos\left((2n+1)\frac{\pi y}{L}\right) \exp\left\{-\frac{\sigma_0^2}{2} [(2m+1)^2 + (2n+1)^2] \frac{\pi^2}{L^2}\right\} \delta\left(t - \frac{j}{R} - \frac{q}{\nu}\right). \quad (\text{S2})$$

The sums in n, m are taken over Fourier modes that vanish at the boundary, truncated to orders $M, N = 10$.

We solve the inhomogeneous problem Eq. (S1) by first solving for the response $T_0(x, y, t; \alpha, A, \sigma_0)$ to a single forcing pulse, treated as a homogenous problem with the forcing term accounted for in the initial conditions. The linearity of Eq. (S1) then entails that,

$$T(x, y, t; \alpha, A, \sigma_0) = \sum_{q=-\infty}^{\infty} \sum_{j=0}^{J-1} T_0\left(x, y, t - \frac{j}{R} - \frac{q}{\nu}; \alpha, A, \sigma_0\right). \quad (\text{S3})$$

It is well known that for a single spatial Fourier mode $\hat{T}(k, t)$, the solution to the homogenous heat equation is,

$$\hat{T}(k, t) = \hat{T}(k, 0)e^{-\alpha t k^2}. \quad (\text{S4})$$

For the first impulse we therefore obtain,

$$T_0(x, y, t; \alpha, A, \sigma_0) = \frac{4A}{L^2} \sum_{m=0}^{M-1} \sum_{n=0}^{N-1} \cos\left((2m+1)\frac{\pi x}{L}\right) \cos\left((2n+1)\frac{\pi y}{L}\right) \exp\left\{-\frac{1}{2}(\sigma_0^2 + 2\alpha t) [(2m+1)^2 + (2n+1)^2] \frac{\pi^2}{L^2}\right\}. \quad (\text{S5})$$

Having in hand the expression for T_0 on the right hand side of Eq. (S5), to compute the sums in Eq. (S3), we first approximate the sum inside each train as an integral. It is convenient to define three expressions that appear at intermediate steps in the computation,

$$E_{mn}(t; \alpha) := \exp\left\{-\alpha t [(2m+1)^2 + (2n+1)^2] \frac{\pi^2}{L^2}\right\}, \quad (\text{S6})$$

$$P_{mn}(t; \alpha) := E_{mn}(t; \alpha) * \sum_{j=0}^{J-1} \delta(t - j/R), \quad (\text{S7})$$

and,

$$\tilde{P}_{mn}(t; \alpha) := \sum_{q=-\infty}^{\infty} P_{mn}(t - q/\nu). \quad (\text{S8})$$

The approximating integral is then performed piece-wise in time, first for $t < J/R$, inside the pulse train,

$$P_{mn}(t; \alpha) = R \int_0^t E_{mn}(\tau; \alpha) d\tau \quad (\text{S9})$$

$$= \frac{L^2 R}{\alpha \pi^2 [(2m+1)^2 + (2n+1)^2]} [1 - E_{mn}(t; \alpha)] \quad (\text{S10})$$

Then, after the pulse train has ended, for $t \geq J/R$:

$$P_{mn}(t; \alpha) = \frac{L^2 R}{\alpha \pi^2 [(2m+1)^2 + (2n+1)^2]} [1 - E_{mn}(J/R; \alpha)] E_{mn}(t - J/R). \quad (\text{S11})$$

The remaining sum over all pulse trains can be computed using the formula for a geometric series to give, for $t < J/R$:

$$\begin{aligned} \tilde{P}_{mn}(t; \alpha) &= \frac{L^2 R}{\alpha \pi^2 [(2m+1)^2 + (2n+1)^2]} \left\{ 1 - E_{mn}(t; \alpha) \right. \\ &\quad \left. + [1 - E_{mn}(J/R; \alpha)] E_{mn}(t - J/R; \alpha) \sum_{j=1}^{\infty} \exp \left\{ \right. \right. \\ &\quad \left. \left. - \frac{1}{2} \alpha j [(2m+1)^2 + (2n+1)^2] \frac{\pi^2}{f L^2} \right\} \right\} \quad (\text{S12}) \end{aligned}$$

$$\begin{aligned} &= \frac{L^2 R}{\alpha \pi^2 [(2m+1)^2 + (2n+1)^2]} \left\{ 1 - E_{mn}(t; \alpha) \right. \\ &\quad \left. + [1 - E_{mn}(J/R; \alpha)] \frac{E_{mn}(t - J/R; \alpha)}{E_{mn}(-1/\nu; \alpha) - 1} \right\}, \quad (\text{S13}) \end{aligned}$$

and for $t \geq J/R$,

$$= \frac{L^2 R}{\alpha \pi^2 [(2m+1)^2 + (2n+1)^2]} [1 - E_{mn}(J/R; \alpha)] \frac{\tilde{P}_{mn}(t; \alpha) E_{mn}(t - J/R; \alpha)}{1 - E_{mn}(1/\nu; \alpha)}. \quad (\text{S14})$$

The fit function expressed in terms of the \tilde{P}_{mn} is therefore,

$$\begin{aligned} T(x, y, t; \alpha, A, \sigma_0) &= \\ &= \frac{4A}{L^2} \sum_{m=0}^{M-1} \sum_{n=0}^{N-1} \cos \left((2m+1) \frac{\pi x}{L} \right) \cos \left((2n+1) \frac{\pi y}{L} \right) \tilde{P}_{mn}(t; \alpha) \exp \left\{ \right. \\ &\quad \left. - \frac{1}{2} \sigma_0^2 [(2m+1)^2 + (2n+1)^2] \frac{\pi^2}{L^2} \right\}. \quad (\text{S15}) \end{aligned}$$